[19]F MRI of Polymer Nanogels Aided by Improved Segmental Mobility of Embedded Fluorine Moieties

Oyuntuya Munkhbat[1], **Mine Canakci**[2], **Shaokuan Zheng**[3], **Weiguo Hu**[4], **Barbara Osborne**[2,5], **Alexei A. Bogdanov**[3], and **S. Thayumanavan**[1,2,5]

[1]Department of Chemistry, University of Massachusetts, Amherst, Massachusetts 01003, United States

[2]Molecular and Cellular Biology Program, University of Massachusetts, Amherst, Massachusetts 01003, United States

[3]Department of Radiology and the Laboratory of Molecular Imaging Probes, and The Chemical Biology Interface Program, University of Massachusetts Medical School, Worcester, Massachusetts 01655, United States

[4]Department of Polymer Science and Engineering, University of Massachusetts, Amherst, Massachusetts 01003, United States.

[5]The Center for Bioactive Delivery, Institute for Applied Life Sciences, University of Massachusetts, Amherst, Massachusetts 01003, United States

Abstract

Using fluorinated probes for ^{19}F MRI imaging is an emerging field with potential utility in cellular imaging and cell tracking *in vivo*, which complements conventional ^{1}H MRI. An attractive feature of ^{19}F-based imaging is that this is a bio-orthogonal nucleus and the naturally abundant isotope is NMR active. A significant hurdle however in the ^{19}F MRI arises from the tendency of organic macromolecules, with multiple fluorocarbon substitutions, to aggregate in the aqueous phase. This aggregation results in significant loss of sensitivity, because the T_2 relaxation times of these aggregated ^{19}F species tend to be significantly lower. In this report, we have developed a strategy to covalently trap nanoscopic states with an optimal degree of ^{19}F substitutions, followed by significant enhancement in T_2 relaxation times through increased segmental mobility of the side chain substituents facilitated using stimulus-responsive elements in the polymeric nanogel. In addition to NMR relaxation time based evaluations, the ability to obtain such signals are also evaluated in mouse models. The propensity of these nanoscale assemblies to encapsulate hydrophobic drug molecules and the availability of surfaces for convenient introduction of

Corresponding Authors alexei.bogdanov@umassmed.edu, thai@chem.umass.edu.

ASSOCIATED CONTENT

The Supporting Information is available free of charge on the ACS Publications website at https://pubs.acs.org. Detailed synthetic protocols of monomers and polymers; characterization (^{1}H NMR, ^{13}C NMR, ^{19}F NMR, GPC and DLS) of small molecules and polymers; T_2 curve fittings; additional ^{1}H and ^{19}F MR images.

Notes

fluorescent labels suggest the potential of these nanoscale architectures for use in multi-modal imaging and therapeutic applications.

Graphical Abstract
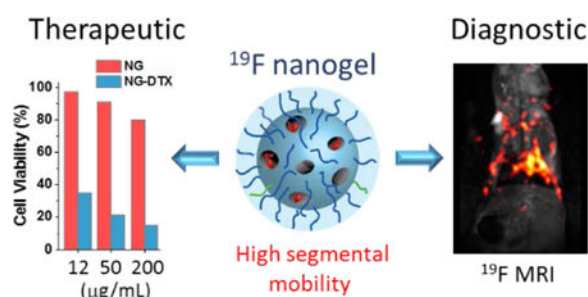
Keywords

^{19}F MRI; amphiphilic polymers; fluorinated polymers; T_2 relaxation time enhancement

INTRODUCTION

Cellular and tissue imaging techniques, especially those based on magnetic resonance imaging (MRI), have gained much prominence in current clinical and biomedical research, because of their non-invasive nature and the resultant patient compliance. Among the nuclei that are probed for this purpose, ^{19}F MRI has emerged as a field that holds great promise in multimodal imaging of targeted drug delivery and cell therapy. [1–3] The ^{19}F nucleus exhibits excellent NMR sensitivity, owing to its favorable magnetic properties that are quite close to that of ^{1}H, but with essentially no detectable background signal in the human body. Thus, the signal intensity is a direct consequence of the presence of the fluorinated probe and the anatomical localization of fluorine-containing particles or cells that can be identified precisely when the ^{19}F MR image is superimposed with ^{1}H density image.[4,5]

The promise of ^{19}F MRI was particularly recognized, following the proof-of-principle demonstration of *in vivo* cell tracking of immune cells using perfluorocarbon (PFC) nanoemulsions.[6–8] However, complex formulation, droplet instability, and the lack of facile functionalization of PFCs have limited their full reach in potential applications in targeted therapeutics and theranostics.[3,9,10] Polymeric contrast agents (CAs) present an advantage in terms of attaining high fluorine content with sharp ^{19}F NMR peak, which is necessary for obtaining reduced chemical shift image artifacts, and thus high sensitivity.[11] In this vein, recent efforts have focused on developing polymeric ^{19}F MRI contrast agents as multimodal imaging probes. A variety of polymeric tracers have been developed and tested, including linear polymers,[12–19] star polymers,[20,21] dendritic polymers,[22–24] hyperbranched polymers (HBPs),[25–29] and polymeric nanoparticles.[30–32] In addition, there also have been efforts to develop activatable "smart" agents that provide on-off ^{19}F signals in response to certain environmental changes, such as pH, redox potential, small molecule release and proteins.[17,30,33–37]

The key challenge in fully realizing the potential of polymeric tracers for these applications arises from the fact that fluorocarbon substitutions render segments of polymers hydrophobic, which leads to aggregation. This aggregation process has deleterious effects on their use in ^{19}F MRI applications. An ideal polymeric tracer should possess relatively short T_1 relaxation time for minimum scan time and sufficiently long T_2 relaxation time for high signal intensity. Both T_1 and T_2 are influenced by molecular motion, particularly T_2. Spin-spin relaxation time of fluorine is sensitive to spatial arrangements and mobility of the nuclear spins, since it is defined by the dipolar coupling between neighboring ^{19}F and ^{1}H nuclei. Consequently, fluorine signal intensity is significantly attenuated in an aqueous environment due to the aggregation-induced loss of molecular mobility and the subsequent decrease in T_2 relaxation time.[38] Therefore, an ideal polymeric tracer would be characterized by high number of fluorine moieties, where there is significant segmental mobility and the fluorine-fluorine interaction is kept to a minimum.[3,39] Considerable efforts have been taken to address this challenge by varying molecular architectures (hyperbranched, random vs. block copolymers),[25,28,29,38] engineering electrostatic repulsions among polymer chains,[13,20,30] and modulating the glass transition temperature (T_g) of the polymer.[12] Despite these exciting advances, significant improvements in T_2 are still required for practical use in *in vivo* applications.

We envisaged an approach in which one can take advantage of the hydrophobic properties of the fluorocarbon substituents promote the self-assembly of amphiphilic polymers into nanoscale aggregates, the fluorocarbon-bearing interior density of which is then manipulated in a post-assembly step. Such a strategy consists of three steps: (*a*) formation of polymeric assembly with high fluorocarbon core, along with degradable hydrocarbon moieties; (*b*) preservation of the assembly through chemical crosslinking; (*c*) triggered degradation of cleavable hydrocarbon parts to decrease the density of the assembly's interior. We show here that such an assembly exhibits increased T_2 relaxation time and results in enhanced signal intensities in ^{19}F NMR and ^{19}F MRI phantom imaging. In vivo MRI imaging capability of these nanogels were also assessed in mouse models.

EXPERIMENTAL SECTION

Monomer and Polymer Synthesis.

Random copolymers were synthesized via either AIBN radical polymerization or RAFT polymerization technique using commercially available and custom synthesized acrylate monomers. Detailed procedure for preparation and the characterization of each monomer and polymer are available in supplementary information.

Nanogel Preparation and Characterization.

Polymer micelles were prepared by direct dissolution of amphiphilic polymers in PBS buffer (10 mM, pH 7.4) at 20 mg/mL concentration. Crosslinked polymer nanogels were synthesized by addition of deficient amount of DTT into polymer micelle solution. To a vial containing 2 mL of 20 mg/mL polymer solution that had previously encapsulated hydrophobic dye molecule (DiI) added 20 μL of 45.3 mg/mL DTT solution. Crosslinking reaction was monitored with the UV absorption spectrometer by following the absorption

maximum of byproduct, 2-pyridothione, at 343 nm. Crosslink density was calculated by using the molar extinction coefficient of byproduct (8.08×10^3 M^{-1}cm^{-1} at 343 nm). Size distribution of polymer nanoparticles were measured with Malvern Nanozetasizer-ZS. All samples were diluted to 1 mg/mL with PBS buffer (10mM) and filtered through 0.22 μm syringe filter prior to measurement. Hydrodynamic diameters provided are volume averages of three measurements.

Hydrophobic Dye (DiI) Encapsulation.

To a vial containing 2 mL of 20mg/mL polymer solution in PBS buffer (10mM) added 40 μL of 10 mg/mL DiI (1% wt feed) in acetone, followed by evaporation of acetone by leaving the vial uncapped for 6 hours while stirring at room temperature. After 6 hours, the volume of polymer solution is reconstituted back to original 2 ml with the addition of PBS buffer. Non-encapsulated excess DiI has been removed by 0.22 μm pore size syringe filter.

Hydrophobic Drug (DTX) Encapsulation.

To a vial containing 1 mL of 20mg/mL polymer solution in PBS buffer (10mM) added 60 μL of 66.7 mg/mL docetaxel (20% wt feed) in acetone, followed by evaporation of acetone by leaving the vial uncapped for 10 hours while stirring at room temperature. After 10 hours, the volume of polymer solution is reconstituted back to original 1 ml with the addition of PBS buffer. Non-encapsulated excess docetaxel has been removed by 0.22 μm pore size syringe filter.

Surface modification of crosslinked nanogel with FITC-SH.

0.4 mg (1% wt. feed) of FITC-SH was dissolved in minimum amount of DMSO (50 μL) and added to the 2 mL of previously crosslinked nanogel solution (20 mg/mL). After stirring for 2h in ambient condition, excess FITC-SH, DMSO and 2-pyridothione were removed by dialysis against PBS buffer. FITC-SH conjugation is quantified by UV-Vis spectroscopy based on the FITC absorbance at 498 nm using the molar extinction coefficient of 75800 M^{-1} cm^{-1} and found to be 0.08% wt.

Surface modification of crosslinked nanogel with FITC-SH and FA-SH.

0.4 mg (1% wt. feed) of FITC-SH was dissolved in minimum amount of DMSO (50 μL) and added to the 2 mL of previously crosslinked nanogel solution (20 mg/mL). After stirring for 1h, 0.4 mg (1% wt. feed) of FA-SH in 50 μL DMSO was added to the reaction mixture and stirred for another 1h. Finally, unreacted FITC-SH, FA-SH, DMSO and 2-pyridothione were removed by dialysis against PBS buffer. FA-SH conjugation is quantified by UV-Vis spectroscopy based on the folic acid absorbance at 344 nm using the molar extinction coefficient of 7150 M^{-1} cm^{-1} and found to be 0.8% wt.

^{19}F NMR Measurement.

^{19}F NMR spectra of polymers in organic solvent (CDCl3) and PBS/D$_2$O (90/10, v/v) were acquired using Bruker 500 MHz NMR spectrometer. All polymers samples in PBS buffer were originally prepared in 20 mg/mL concentration and diluted to 17.8 mg/mL with 10%

D$_2$O. NMR measurements are performed with following parameters: 90°C pulse width 12.5 s, with 32 scans.

T$_1$ Relaxation Time Measurement.

T$_1$ relaxation time of all polymers in CDCl$_3$ and PBS/D$_2$O (90/10, v/v) were measured by using standard inversion-recovery pulse sequence in Bruker 500 MHz NMR spectrometer. All polymer samples in PBS buffer were originally prepared in 20 mg/mL concentration and diluted to 17.8 mg/mL with 10% D$_2$O prior to measurement. ^{19}F NMR acquisitions are performed with recovery times ranging from 1 ms to 5 s, 90°C pulse width 12.5 s, relaxation delay of 2.5 s with 16 scans. Only peak intensities for major peak at around −72.23 to −72.29 were used for exponential functions for the estimation of T$_1$.

T$_2$ Relaxation Time Measurement.

T$_2$ relaxation times were measured using Carr-Purcell-Meilboom-Gill (CPMG) pulse sequence in Bruker 500 MHz NMR spectrometer. T$_2$ of all polymer samples both in CDCl3 and PBS/D$_2$O (90/10, v/v) were acquired. For each measurement, 16 data points were recorded with echo times ranging from 3 to 240 ms, which were then analyzed by Dynamic Center Software to estimate T$_2$ relaxation times. ^{19}F NMR acquisitions were performed with 90°C pulse width 12.5 s, with 16 scans.

Diffusion NMR.

Diffusion NMR of samples P1 and P1H were conducted by using a bipolar-gradient, stimulated echo pulse sequence on a Bruker 400 MHz NMR spectrometer at 25°C. Samples in PBS buffer were originally prepared in 20 mg/mL concentration and diluted to 17.8 mg/mL with 10% D$_2$O prior to measurement. The fittings of diffusion data were performed using OriginPro 2017. The data for both samples could be well fitted with a two-component exponential function, with reduced R^2 of 0.99999 and 0.99998 for P1 and P1H, respectively. Hydrodynamic diameters were calculated using the Stokes-Einstein equation from the diffusion coefficient of each component.

^{1}H and ^{19}F MRI Phantom Imaging.

All ^{1}H and ^{19}F MRI phantom experiments were performed in a 3T (128 MHz for 1H) Achieva whole-body MRI scanner (Philips Medical Systems, Best, Netherlands) by using a custom-made solenoid (either 5mm or 35mm diameter) T/R coil and modular ^{19}F Gateway Interface (Clinical MR Solutions, LLC Brookfield, WI). Either standard 5mm NMR spectroscopy tubes (Figure S27) or 0.2 mL polypropylene PCR tubes (Figure S28) were used for phantom imaging. A 3D ultrashort echo time (UTE) pulse sequence was used to acquire ^{19}F MR images to maximize signal from ^{19}F, which has a very short T2, and thus rapidly decaying MR signal. The ^{19}F MR images of polymer solutions were acquired by using UTE (TR/TE=600/0.13 ms; FA= 65°), 6 slices; voxel size=1×1×4 mm, field of view (FOV) of 24 mm × 24 mm. Raw images were imported and processed using ImageJ. Signal-to-noise ratios were calculated by normalizing the region-of-interest mean intensity values by standard deviation of signal noise.

^{1}H and ^{19}F MRI Animal Imaging.

All animals were housed in the animal facilities complied with the guidelines approved by of the Institutional Animal Care and Use Committee at the University of Massachusetts, Worcester, MA. All ^{1}H and ^{19}F animal experiments were performed using same custom-made 35mm diameter solenoid T/R coil at 3.0 T. The coil was first tuned to the proton resonant frequency to acquire ^{1}H images and then re-tuned to ^{19}F resonant frequency to acquire ^{19}F images. A turbo spin echo (TSE) pulse sequence was used for both ^{1}H and ^{19}F imaging. The ^{1}H imaging parameters for T1-weighted imaging were: 6 slices with slice thickness of 4 mm; field of view (FOV) = 24 mm × 30.6 mm × 50 mm with; TSE factor=8; TR/TE = 600/13 ms; Same geometric parameters were used for T2-weighted ^{1}H imaging, other imaging parameters were: TSE factor=8; TR/TE = 3000/70 ms; Subsequently, the coil was re-tuned to ^{19}F resonant frequency and ^{1}H images were used to plan the ^{19}F MR imaging plane. Feasibility ^{19}F MR images were acquired by using TSE pulse sequence with following parameters: TSE factor=8; TR/TE = 1000/4.4 ms; flip angle (FA) = 90°; NSA = 39; same geometric parameters as ^{1}H imaging was used for ^{19}F imaging.

Cell culture.

HeLa (human cervical adenocarcinoma) were obtained from the American Type Culture Collection (ATCC ID: CCL-2). Cells were cultured in Dulbecco's Modified Eagle's medium/F12 (DMEM/12) supplemented with 2 mM L-glutamine, 10 μg/mL streptomycin, 100 U/mL penicillin and 10% (v/v) fetal bovine serum (FBS) at 37 °C in a humid atmosphere of 10% CO_2. When HeLa cells were grown to 90% confluency, cells were trypsinized for 5 mins in PBS and passaged 1:10 into a new tissue culture plate. Maximum number of passage was limited to 10 for HeLa cells. DMEM/F12 and supplements were obtained from ThermoFisher.

MTT Assay.

For cell viability assay, HeLa cells were trypsinized and counted. Cells were seeded on flat bottom 96-well tissue culture plates at a density of 7,000 cells/well and rested for 24 hours at 37 °C in 10% CO_2. After overnight incubation, the culture medium was removed, and cells were treated with empty or docetaxel loaded nanogel samples at different concentrations in complete medium for 24 hours. After treatments, cells were washed, and fresh medium was added. Cells were incubated with the fresh medium for further 24 hours. Next day, medium was replaced with 3-(4,5-dimethylthiazol-2-yl) 2,5-diphenyltetrazolium solution (MTT) (prepared as 1 mg/mL in medium) and cells were incubated for 3–4 hours at 37 °C to allow the formation of the MTT formazan. 96-well plate was spun for 5 minutes to let the formazan settle at the bottom of the plate. MTT medium was discarded and formazan was dissolved in 100 μL of DMSO. Purple color formation was observed and recorded using a plate reader at 540nm.

Confocal Microscopy.

Confocal experiment was performed with Nikon A1 Spectral Detector Confocal (IALS, UMASS, Amherst). HeLa cells were cultured in MatTek glass bottom dishes until they reached the 70% confluency. DiI loaded NG samples were diluted to 0.25 mg/mL in

complete medium and incubated with cells for 2 hours at 37 °C in 10% CO2. Later, cells were washed with cold PBS at least three times and samples were fixed with 3% paraformaldehyde. Nucleus were stained with NucBlue (Thermofisher) and plasma membrane were stained with CellMask Deep Red (Thermofisher). The Images were analyzed using NIS-Elements Software.

RESULTS AND DISCUSSION

Design, Synthesis and Assembly Formation of pH-responsive Multimodal Imaging Probes.

Consistent with the strategy outlined above, we designed an amphiphilic random copolymer that consists of both crosslinkable functionalities and degradable hydrophobic moieties, in addition to the fluorocarbon probe. Our approach to generate interior flexibility of amphiphilic assembly was based on preserving the morphology through chemical crosslinking first and then degrading and removing the cleavable portions from the interior of the crosslinked nanogel. To achieve this, we used the *in situ* crosslinking based nanogel formation strategy.[40–42] We ascertained that incorporation of up to 30% of the hydrophilic oligoethylene glycol (OEG) based monomer in amphiphilic polymers offers robust aggregate formation. We also chose 15% crosslinking as the starting point, which was accomplished by incorporating ~15% of the pyridyldisulfide (PDS) based hydrophobic monomer in the polymer. The remaining 55% of the repeat units is used for optimizing the balance between the fluorocarbon probe moiety and the acid-degradable tetrahydropyranyl (THP) moieties. Note that the balance between these two moieties is likely to be the key determinant in achieving high fluorine content and high segmental mobility. The fluorine content is achieved by merely increasing the percentage of fluorocarbon moieties, while the segmental mobility is achieved by the decreased density of the nanogel's interior, facilitated by the acid-catalyzed removal of the THP (Figure 1).

Three different polymers (**P1**-**P3**) with constant ratio of OEG:PDS (30%:15%) units and varying ratios of THP:CF$_3$ units were synthesized. We systematically increased the molar ratio of fluorine content from 10% to 20% and to 30% in **P1**-**P3** respectively, where the molar ratio of the acid-labile THP group decreased from 45% to 35%, and to 25%. To evaluate the importance of acid-labile responsive group in molecular design, we included a control polymer (**PC**) into our library that lacks the acid-labile THP group. Instead, **PC** contains cyclohexyl acrylate moiety, which is structurally close to THP but is not responsive to acidic pH (Figure 2). Polymer **PC** contains same ratio of OEG:PDS (30%:15%) as all other polymers, and 25% of cyclohexyl and 30% of CF3. Another interesting control that can test the significance of degradable moiety is to include **P6** in our library, in which there are no THP or the phantom-cyclohexyl groups.

In addition, we were interested in exploring the properties of polymers that contain structurally different fluorine monomers to elucidate the effects of fluorinated aromatics, as well as the density of fluorocarbon substituents. In these cases, we also imposed that all fluorine moieties should be chemically equivalent (from the side chain perspective), in order to achieve NMR signals with similar chemical shifts. For this purpose, we designed and synthesized polymers **P4** and **P5** (Figure 2). **P4** contains 6 equivalent aromatic fluorine

moieties within the monomer, while **P5** and **P1** contain 27 and 3 equivalent aliphatic fluorines within the monomer unit respectively.

All polymers were successfully synthesized and characterized by NMR and GPC (see Supplementary Information for details). Based on the feed ratio of monomers, P1, P2 and P3 are expected to have PDS and THP groups in ratios around 1:3, 1:2.33 and 1:1.67. According to NMR characterization of polymers, these ratios are found to be 1:2.44, 1:1.95 and 1:28. Assemblies were conveniently prepared in PBS buffer (10 mM, pH=7.4) and the average hydrodynamic radius was measured using dynamic light scattering (DLS). Polymers formed small size assemblies with narrow distribution of **P1**, **P2**, **P3** and **PC** having 6, 8, 9 and 14 nm, respectively (Figure 3e and Table S1 and Table S2). The polymer assemblies were chemically crosslinked with the addition of dithiothreitol (DTT) to yield the corresponding polymer nanogels (**P1X**, **P2X**, **P3X** and **PCX**). We use 0.5 equivalent of DTT (with respect to the PDS moieties) to convert 50% of the PDS groups to free thiols. These thiols then react with the remaining PDS moieties to generate a fully crosslinked polymeric nanogel. The extent of this reaction was monitored and confirmed by the release of water soluble byproduct, 2-pyridothione, through its characteristic absorption peak at 342 nm (Figure 3a and 3b). Once the nanogels are formed, partial degradation of hydrophobic interior was achieved by the addition of HCl to hydrolyze the acid-responsive THP groups to achieve the final, degraded nanogels **P1H**, **P2H**, **P3H** and **PCH**. No drastic change in size and nanogels composition was observed throughout the whole process. There is a slight increase in size observed after acid degradation for pH-responsive polymers, which is likely due to the electrostatic repulsion of resultant anionic side chains at neutral pH (Figure 3e and 3f).

^{19}F NMR Analysis.

Spin-spin (T_2) and spin-lattice (T_1) relaxation times of fluorine nuclei are the parameters that closely reflect molecular mobility of perfluorinated moieties. The observed MR signal is a function of these parameters that reflect the performance of ^{19}F MRI probe. Hydrophobic aggregation of fluorine probe restricts the local motion of ^{19}F nuclei and heavily influences these relaxation times, especially T_2. As a result, the successful use of ^{19}F MRI probe is complicated by the aggregation induced signal attenuation and by the loss of signal intensity in aqueous milieu. This phenomenon is evident in our current amphiphilic polymer systems as well. When polymers are dissolved in chloroform without self-assembly, the fluorine segments are completely flexible, which generates a single sharp peak at ~−73.2 ppm in ^{19}F NMR for polymers bearing CF3 monomer (**P1**-**P3**, **PC** and **P6**), ~−62.8 ppm for **P4**, ~−70.4 ppm for **P5**. T_2 times of **P1**, **P2**, **P3** and **PC** in chloroform were found to be 141, 153, 160 and 193 ms, respectively. However, when polymers were dissolved in a biologically relevant milieu, such as the PBS buffer, a drastic decrease in relaxation time is observed, specifically in T_2, presumably due to solvophobicity driven self-assembly. This phenomenon is evident in all polymer assemblies, but much more significant in polymers that contain aromatic fluorine monomers (**P4**) as well as in polymers with high fluorine density (**P5**). ^{19}F NMR peaks in aqueous solution were very weak and T_2 relaxation times were too short to accurately measure it in these two polymers (Figure S22). These results indicate that the fluorine monomers with aromatic structure or with higher fluorine density are not ideal for

achieving higher mobility in these types of systems. This is understandable, as amphiphilic assemblies driven by aromatic units have been shown to exhibit significant increase in aggregate stability.[43] This explanation is further supported with our observation with **P6**, where the observed low T2 of 7 ms could be attributed to the highly aromatic rigid core associated with unused PDS groups that decreased the chain flexibility.

Although the assemblies of **P1**-**P3** in PBS/D_2O (90:10, v/v) presented peak broadening in ^{19}F NMR due to a decrease in T_2 relaxation time, peak intensities were considerably higher than other polymers with a single peak between −73.11 and −73.28 ppm (Figure 4c and Figure S23). Each of these polymers exhibited three different T_2 values in PBS buffer with varying intensities, suggesting that the polymer aggregation resulted in a three-component system in terms of the fluorine microenvironment. On average, all three polymers exhibited three T_2 relaxation times of ~ 4 ms (60%), ~17 ms (30%), and ~130 ms (10%) (Table 1). This could be due to the broad size distribution of assemblies or due to the varying microenvironments of the fluorine nuclei, ranging from the nanogel core to the corona. To differentiate these possibilities, we conducted diffusion NMR experiments on two of the samples, **P1** and **P1H**. For both samples, the diffusion data slightly deviate from a single-component fit, while could be well-fitted by two-component models (Table S5 in SI). Note that the distribution of nanogel particle sizes is continuous, thus the two-component fit does not suggest that there are only two sizes of the particles in each sample, but rather that most of the nanogel particles fall between the two sizes. For **P1** and **P1H**, most particles fall between the hydrodynamic diameters of 3.6 and 9.8 nm, and 4.4 and 12.6 nm, respectively. These results agree very well with DLS measurements. Since T_2 is approximately proportional to the correlation time of the underlying dynamics, and the correlation time of the particle's tumbling motion is inversely proportional to its hydrodynamic diameter, the narrow particle size distribution as observed by diffusion NMR and DLS would not be able to account for the factor of ~30 difference between the T_2's of the various components. Therefore, the multi-component T_2 is most likely due to the distribution of fluorine microenvironment within the nanogel particles (Figure 4d). The T_2 values of the short-T_2 component (~4 ms) are very similar for **P1**-**P3** and **PC**. For **PC**, which is the most hydrophobic among all four samples, the short-T_2 component is the dominant one. Therefore, we could assign this component to the CF_3 that is inside the hydrophobic core, which has low mobility. The T_2 values of the long-T_2 component (~130 ms) are similar for **P1**-**P3** both in PBS buffer and in chloroform and for all their crosslinked and hydrolyzed derivatives, which suggests that the long-T_2 component can be assigned to the hydrated and mobile corona, in which the CF_3 is sandwiched between hydrophilic comonomers, and has high mobility. The intermediate-T_2 component (~17 ms) may be assigned to the surface of the hydrophobic cores and smaller hydrophobic clusters, which has a mobility that is in between the hydrophobic core and the hydrophilic corona.

Crosslinking and hydrolysis change the relative populations of the three components, while their T_2 values stay mostly constant. This indicates that crosslinking and hydrolysis did not drastically alter the morphology of the nanogel particles. Average value of T_2 for polymer assemblies were calculated based on the respective intensity ratios and found to be 21, 20, and 21 ms for **P1**, **P2**, and **P3**, respectively. It is noteworthy that the T_2 of longest relaxing

component is the highest in **P3** (146 ms, 9.5%) compared to **P1** (130 ms, 9.8%) and **P2** (119 ms, 11.3%), but the value is offset by the large fraction of shortest relaxing component of **P3** (3.8 ms, 65.5%). The opposite trend holds true for **P1**, where the average T_2 becomes similar to **P2** and **P3** in spite of its low value of long relaxing component that is compensated by the lower fraction of short relaxing fluorine nuclei of **P1** (4.3 ms, 56.7%). At last, the strongest effect on T_2 due to association of fluorine is observed in control polymer, **PC**, in which the relaxation time is decreased from 193 ms to 5.1 ms having 94% of 3 ms component out of two.

Finally, note that T_1 relaxation times for all polymers decreased from ~520 ms to ~ 360 ms. As we discussed earlier, short T_1 is desired for attaining strong signal in MRI. Therefore, decrease in T_1 relaxation time impacts the overall imaging positively by shortening scan time and improving signal to noise ratio.

Next, we investigated the change in relaxation times upon acid degradation of nanogels. But prior to the acid hydrolysis, stabilization of polymer assembly through crosslinking is essential. Otherwise, the polymer assembly may lose its nanoparticle morphology due to the loss of hydrophilic-lipophilic balance after acid degradation of hydrophobic THP groups. We expected a slight decrease in T_2 relaxation time upon mild crosslinking since it has been previously shown that the high degree of branching reduced the chain flexibility in HBPs.[38] However, average T_2 relaxation times of nanogels increased slightly to 27, 24, and 24 ms for **P1X**, **P2X**, and **P3X**, respectively. This is ascribed to the consumption of PDS groups during the crosslinking reaction. Although the core of the nanoparticle is rigidified through chemical crosslinking, cleavage of hydrophobic PDS groups minimizes the overall hydrophobicity and increases the segmental flexibility. Similar trend is observed for **PCX**, whose average T_2 is increased from 5.1 ms to 6.1 ms. Small changes in both T_2 value and respective ratios of each component contributed to the final evolution of average T_2.

Acid hydrolysis of THP was carried out at pH 2 for 4 hours followed by the addition of base. Base addition was used to bring back the pH to 7.4 and trigger the deprotonation of acrylic acid moieties. The ratio of degradable moiety is varied from 45% to 35% and to 25% in **P1**, **P2**, and **P3**, while the ratio of fluorine is increasing from 10% to 20% and to 30%, respectively. Since **P1** has the highest amount of acid labile group, the highest level of enhancement in segmental mobility is expected. Indeed, we observed an increase in average T_2 by more than a factor of two for **P1** (21 ms to 54 ms), which is much higher than those for **P2** and **P3** (Figure 5a). The relative change within the three components of T_2 was also analyzed. After acid degradation, the shortest relaxing component of **P1** increased from 4.3 ms to 10.4 ms at the same time the relative ratio is decreased from 56.7% to 33.7% whereas both value and ratio of medium relaxing and long relaxing components increased from 16.2 (32%) ms to 37.8 ms (44.5%) and from 119 ms (11.3%) to 155 ms (21.8%), respectively. We observed the same trend of T_2 enhancement for each component for **P2** and **P3** except the extent of increase was less than in **P1**, indicating that the internal flexibility is improved by the removal of THP groups in a ratio dependent manner. However, it is noted that the difference in enhancement between **P2** and **P3** was found to be quite small, suggesting that the ratio-dependent enhancement has peaked between **P1** and **P2**. This phenomenon is

confirmed by the studies on control polymer, **PC**, where the T_2 was indeed decreased from 5.1 ms to 3.9 ms.

There is no significant change in T_1 observed for all polymers during the crosslinking and the acid treatment. All polymers before and after acid treatment exhibited only one T_1 relaxation value within same range, meaning that the change in interior plasticity and conformational mobility do not affect the spectral density of fluorine nuclear spins (Figure 5b).

^{19}F MRI Phantom and Animal Imaging.

To test the potential contrast enhancement in ^{19}F MRI, we conducted phantom imaging analysis first. Polymer assemblies showed strong signal in phantom imaging at 15 mM fluorine concentration using ultrashort TE pulse sequence (UTE) acquisition of ^{19}F MR signal with 3T Philips Achieva MRI scanner (Figure S27). Samples were scanned in an NMR tube by using a 5 mm diameter transmit/receive RF coil. To accommodate several samples simultaneously, for comparative imaging of ^{19}F-specific resonances, we used a larger diameter (35 mm diameter) solenoid transmit/ receiver coil resulting in a decrease in the overall ^{19}F signal intensity. However, the MR signal measured in each of four samples provided high enough signal-to-noise ratio at 20 mg/mL polymer concentration, allowing reasonable signal intensity for each sample. Since the highest T_2 enhancement was observed in **P1**, ^{19}F MR imaging were first conducted on **P1**. At 22 mM concentration of **P1**, there was no appreciable increase in signal intensity, which could be due to the low ^{19}F content in **P1** (Figure S28). Although the flexibility of polymer interior improved, signal intensity did not benefit from this feature, as **P1H** has small amount of ^{19}F. In contrast, MRI signal intensity of **P3** increased 25% upon acid degradation, as shown in Figure 5c and 5d. Despite the same ^{19}F concentration (67 mM) was used, signal intensity in **P3H** is greater than **P3**, **P3X** and **PC**, suggesting that the MRI signal intensity of the polymer nanogel was actually improved by reducing the density of hydrophobic interior via removal of stimuli-responsive side chain. Note however that the UTE pulse sequence is not considered to be sensitive to changes in T_2. Therefore, although interesting, the reason for the intensity increase in **P3H**, relative to other forms of **P3**, is not clear. Nonetheless, it is clear that a critical percentage of fluorine moieties is needed for obtaining a reasonable MR signals in the phantom MRI mode.

To test the feasibility of fluorinated nanogels for animal imaging, intravenous injection of nanogels in mice and subsequent ^{19}F MRI imaging were performed. We continued animal imaging with our most promising polymer, **P3H**, which showed high MRI signal according to phantom imaging. We used a mouse model with induced inflammation as an internal marker, in order to determine whether **P3H** stays in circulation for a prolonged period of time. In two mice (DBA/2) inflammation was induced by injecting lipopolysaccharide (LPS) in Matrigel into the left forepaw shoulder area to keep this site within the field of view during MRI imaging (Figure 5e). These two mice were injected with 0.1 mL of sterile **P3H** polymer nanogel at ~650 mM fluorine concentration and scanned for ^{1}H and ^{19}F MRI after 2 hr and 72 hr time points post injection. In both animals, considerable amount of ^{19}F signal was detected after the 2 hr delay in heart and carotid arteries, indicating that the particles are

abundantly in blood circulation. Signal intensity did not decrease considerably after 72 hours, which demonstrates that these nanogels have long circulation half-life. Also, note that the accumulation of particles around the inflammation area increases over time in each of the animals. This indicates that there might be a propensity for these nanogels to home at the inflammation site. Note however that the current nanogels are not decorated with any targeting moieties to specifically target a tissue type (Figure S29). Nonetheless, these results show the promise of these nanogels for future imaging possibilities.

To show that ^{19}F signal is associated with polymer nanogel, but not with the animal itself, we carried out ^{1}H and ^{19}F MRI imaging for a mouse without any fluid injection. There was no fluorine signal detected during ^{19}F MRI scanning from this animal, indicating that there is no fluorine in the animal body that is sensitive to MRI imaging and the positive signal can be exclusively attributed to the fluorinated polymer nanogels in circulation in the mouse (Figure S30).

Cell targeting and therapeutic delivery of imaging probe.

In addition to the demonstration of the potential utility as a polymeric MRI tracer, we were interested in testing whether the same nanogels can also be used for targeting and as a therapeutic carrier. Such a demonstration would suggest its future for theranostics.[44–48] In addition to the stabilization of polymer assembly formation, the PDS groups also offer a convenient handle for surface functionalization. In this study, nanogels were conveniently functionalized with small amount of folate ligands; folate receptor has been previously shown to be overexpressed in various cancerous tissues.[49–51] In addition to cell targeting ligand, nanogels can be labeled with fluorescent tag molecules that can be used as a handle to monitor the cell uptake by optical microscopy. Thiolated versions of folic acid and fluorescein isothiocyanate (FITC) were sequentially attached to the surface of polymer nanogel by means of thiol exchange reaction with remaining PDS groups. Successful post-conjugation of **P3** is confirmed by the absorption spectrum of polymer nanogel after the extensive dialysis (Figure 6b). Efficient cell uptake of folate decorated nanogels has been shown with folate receptor positive cancer cell line (Figure 6c). To investigate whether the uptake is indeed driven by the folate ligand, a control nanogel was synthesized without the folate ligand. A shown in Figure 6c, the cellular uptake of folate-decorated nanogel was substantially better than the control nanogel. To test whether hydrophobic guest molecules can be noncovalently encapsulated within these nanogels, a hydrophobic cyanine dye, DiI, was incorporated within the nanogel interior. After 2 hr of incubation with HeLa cells, cellular uptake was monitored with by confocal microscopy (Figure 6e-6h), where the presence of the DiI dye is seen in the cytoplasm of the cells. Finally, to further demonstrate the utility of these nanogels, we encapsulated a chemotherapeutic drug molecule, docetaxel (DTX), within the hydrophobic interior of nanogel. We then tested the in vitro cell viability in HeLa cells. As shown in Figure 6d, the drug-loaded **P3** exhibited 50% of cell killing at concentration of ~10 μg/mL whereas there is no significant toxicity by the polymer nanogel itself at the same concentration.

CONCLUSIONS

In summary, we report on a novel polymeric design that has the potential as a multimodal imaging platform, based on ^{19}F MRI imaging. We show here that: (*i*) self-assembly of amphiphilic polymers, driven by the hydrocarbon and fluorocarbon species can be used to embed ^{19}F moieties within a water-soluble polymeric nanoparticle; (*ii*) the NMR and relaxation time loss associated with the reduced segmental mobilities in these aggregates can be mitigated by preserving the morphology of the assembly through crosslinking, followed by release of hydrophobic moieties to increase segmental mobilities within the nanogel interior; (*iii*) MR imaging of the nanogels indicates that a balance between the critical number of fluorine moieties required for MR signals from the polymer and the degree of enhancement in segmental mobility is needed; (*iv*) the ability to decorate these nanogels with fluorophores and utilize their interior to encapsulate drug molecules within their interiors, combined with the inherent biocompatibility of the nanogels, indicate that these nanogels hold promise in multimodal imaging and theranostics applications. Indeed, extending this work in theranostics applications is part our own laboratory's foci.

Supplementary Material

Refer to Web version on PubMed Central for supplementary material.

ACKNOWLEDGEMENTS

REFERENCES

(1). Ahrens ET; Zhong J In Vivo MRI Cell Tracking Using Perfluorocarbon Probes and Fluorine-19 Detection. NMR Biomed. 2013 26 (7), 860–871. [PubMed: 23606473]

(2). Ruiz-Cabello J; Barnett BP; Bottomley PA; Bulte JWM Fluorine (19F) MRS and MRI in Biomedicine. NMR Biomed. 2011, 24 (2), 114–129. [PubMed: 20842758]

(3). Tirotta I; Dichiarante V; Pigliacelli C; Cavallo G; Terraneo G; Bombelli FB; Metrangolo P; Resnati G 19 F Magnetic Resonance Imaging (MRI): From Design of Materials to Clinical Applications. Chem. Rev. 2015, 115 (2), 1106–1129. [PubMed: 25329814]

(4). Janjic J; Ahrens E Fluorine Containing Nanoemulsions for MRI Cell Tracking. Wiley Interdiscip. Rev. Nanomed. Nanobiotechnol. 2009, 492–501.

(5). Ahrens ET; Bulte JWM Tracking Immune Cells In Vivo Using Magnetic Resonance Imaging. Nat. Rev. Immunol.2013, 13 (10), 755–763. [PubMed: 24013185]

(6). Ahrens ET; Flores R; Xu H; Morel PA In Vivo Imaging Platform for Tracking Immunotherapeutic Cells. Nat. Biotechnol. 2005, 23 (8), 983–987. [PubMed: 16041364]

(7). Srinivas M; Morel PA; Ernst LA; Laidlaw DH; Ahrens ET Fluorine-19 MRI for Visualization and Quantification of Cell Migration in a Diabetes Model. Magn. Reson. Med. 2007, 58 (4), 725–734. [PubMed: 17899609]

(8). Srinivas M; Turner MS; Janjic JM; Morel PA; Laidlaw DH; Ahrens ET In Vivo Cytometry of Antigen-Specific T Cells Using 19F MRI. Magn. Reson. Med. 2009, 62 (3), 747–753. [PubMed: 19585593]

(9). Kaneda MM; Caruthers S; Lanza GM; Wickline SA Perfluorocarbon Nanoemulsions for Quantitative Molecular Imaging and Targeted Therapeutics. Ann. Biomedi. Eng. 2009, 37 (10), 1922–1933.

(10). Janjic JM; Srinivas M; Kadayakkara DKK; Ahrens ET Self-Delivering Nanoemulsions for Dual in Vivo Fluorine- 19 MRI and Fluorescence Imaging. J. Am. Chem. Soc. 2008, 130 (9), 2832–2841. [PubMed: 18266363]

(11). Yu YB Fluorinated Dendrimers as Imaging Agents for 19F MRI. Wiley Interdiscip. Rev. Nanomed. Nanobiotechnol. 2013, 5 (6), 646–661. [PubMed: 23929813]

(12). Peng H; Blakey I; Dargaville B; Rasoul F; Rose S; Whittaker AK Synthesis and Evaluation of Partly Fluorinated Block Copolymers as MRI Imaging Agents. Biomacromolecules 2009, 10, 374–381. [PubMed: 19128056]

(13). Nurmi L; Peng H; Seppala J; Haddleton DM; Blakey I; Whittaker AK Synthesis and Evaluation of Partly Fluorinated Polyelectrolytes as Components in 19 F MRI-Detectable Nanoparticles. Polym. Chem. 2010, 1, 1039–1047.

(14). Peng H; Thurecht KJ; Blakey I; Taran E; Whittaker AK Effect of Solvent Quality on the Solution Properties of Assemblies of Partially Fluorinated Amphiphilic Diblock Copolymers. Macromolecules 2012, 45, 8681–8690.

(15). Zhang C; Moonshi SS; Peng H; Puttick S; Reid J; Bernardi S; Searles DJ; Whittaker AK Ion-Responsive F MRI Contrast Agents for the Detection of Cancer Cells. ACS Sens. 2016, 1, 757–765.

(16). Rossi S; Benaglia M; Ortenzi M; Micotti E; Perego C; De Simoni MG Poly(Ethylene-Glycol)-Based Fluorinated Esters: A Readily Available Entry for Novel 19F-MRI Agents. Tetrahedron Lett. 2011, 52, 6581–6583.

(17). Huang X; Huang G; Zhang S; Sagiyama K; Togao O; Ma X; Wang Y; Li Y; Soesbe TC; Sumer BD; et al. Multi-Chromatic PH-Activatable 19F-MRI Nanoprobes with Binary ON/OFF PH Transitions and Chemical-Shift Barcodes. Angew. Chem. Int. Ed, 2013, 52, 8074–8078.

(18). Biaggi C; Benaglia M; Ortenzi M; Micotti E; Perego C; De Simoni MG Easily Available, Low Cost 19F MRI Agents: Poly(Ethylene-Glycol)- Functionalized Fluorinated Ethers. J. Fluorine Chem. 2013, 153, 172–177.

(19). Wallat JD; Czapar AE; Wang C; Wen AM; Wek KS; Yu X; Steinmetz NF; Pokorski JK Optical and Magnetic Resonance Imaging Using Fluorous Colloidal Nanoparticles. Biomacromolecules 2017, 18 (1), 103–112. [PubMed: 27992176]

(20). Wang K; Peng H; Thurecht KJ; Puttick S; Whittaker AK PH-Responsive Star Polymer Nanoparticles: Potential 19F MRI Contrast Agents for Tumour-Selective Imaging. Polym. Chem. 2013, 4, 4480–4489.

(21). Wang KW; Peng H; Thurecht KJ; Puttick S; Whittaker AK Biodegradable Core Crosslinked Star Polymer Nanoparticles as F-19 MRI Contrast Agents for Selective Imaging. Polym. Chem 2014, 5, 1760–1771. h

(22). Ogawa M; Nitahara S; Aoki H; Ito S; Narazaki M; Matsuda T Synthesis and Evaluation of Water-Soluble Fluorinated Dendritic Block-Copolymer Nanoparticles as a 19F-MRI Contrast Agent. Macromol. Chem. Phys. 2010, 211, 1602–1609.

(23). Ogawa M; Nitahara S; Aoki H; Ito S; Narazaki M; Matsuda T Fluorinated Polymer Nanoparticles as a Novel 19F MRI Contrast Agent Prepared by Dendrimer-Initiated Living Radical Polymerization. Macromol. Chem. Phys. 2010, 211, 1369–1376.

(24). Criscione JM; Le BL; Stern E; Brennan M; Rahner C; Papademetris X; Fahmy TM Self-Assembly of PH-Responsive Fluorinated Dendrimer-Based Particulates for Drug Delivery and Noninvasive Imaging. Biomaterials 2009, 30, 3946–3955. [PubMed: 19443028]

(25). Du W; Nyström AM; Zhang L; Powell KT; Li Y; Cheng C; Wickline SA; Wooley KL Amphiphilic Hyperbranched Fluoropolymers as Nanoscopic 19F Magnetic Resonance Imaging Agent Assemblies. Biomacromolecules 2008, 9, 2826–2833. [PubMed: 18795785]

(26). Rolfe BE; Blakey I; Squires O; Peng H; Boase NRB; Alexander C; Parsons PG; Boyle GM; Whittaker AK; Thurecht KJ Multimodal Polymer Nanoparticles with Combined 19F Magnetic Resonance and Optical Detection for Tunable, Targeted, Multimodal Imaging in Vivo. J. Am. Chem. Soc. 2014, 136, 2413–2419. [PubMed: 24437730]

(27). Thurecht KJ; Blakey I; Peng H; Squires O; Hsu S; Alexander C; Whittaker AK Functional Hyperbranched Polymers: Toward Targeted in Vivo 19F Magnetic Resonance Imaging Using Designed Macromolecules. J. Am. Chem. Soc. 2010, 132, 5336–5337. [PubMed: 20345132]

(28). Du W; Xu Z; Nyström AM; Zhang K; Leonard JR; Wooley KL 19F- and Fluorescently Labeled Micelles as Nanoscopic Assemblies for Chemotherapeutic Delivery. Bioconjugate Chem. 2008, 19 (12), 2492–2498.

(29). Fuchs AV; Bapat AP; Cowin GJ; Thurecht KJ Switchable 19 F MRI Polymer Theranostics: Towards in Situ Quantifiable Drug Release. Polym. Chem. 2017, 8, 5157–5166.

(30). Oishi M; Sumitani S; Nagasaki Y On-off Regulation of 19F Magnetic Resonance Signals Based on PH-Sensitive PEGylated Nanogels for Potential Tumor-Specific Smart 19F MRI Probes. Bioconjugate Chem. 2007, 18 (5), 1379–1382.

(31). Oishi M; Sumitani S; Bronich TK; Kabanov AV Boska, MD. Novel 19 F MRS/I Nanoprobe Based on PH-Responsive PEGylated Nanogel: PH-Dependent 19 F Magnetic Resonance Studies. Chem. Lett. 2009, 38 (2), 128–129.

(32). Bailey MM; Mahoney CM; Dempah KE; Davis JM; Becker ML; Khondee S; Munson EJ; Berkland C Fluorinated Copolymer Nanoparticles for Multimodal Imaging Applications. Macromol. Rapid Commun. 2010, 31 (1), 87–92. [PubMed: 21590842]

(33). Mizukami S; Takikawa R; Sugihara F; Hori Y; Tochio H; Wälchli M; Shirakawa M; Kikuchi K Paramagnetic Relaxation-Based 19F MRI Probe to Detect Protease Activity. J. Am. Chem. Soc. 2008, 130, 794–795. [PubMed: 18154336]

(34). Takaoka Y; Sakamoto T; Tsukiji S; Narazaki M; Matsuda T; Tochio H; Shirakawa M; Hamachi I Self-Assembling Nanoprobes That Display off/on 19F Nuclear Magnetic Resonance Signals for Protein Detection and Imaging. Nat. Chem 2009, 1, 557–561. [PubMed: 21378937]

(35). Takaoka Y; Kiminami K; Mizusawa K; Matsuo K; Narazaki M; Matsuda T; Hamachi I Systematic Study of Protein Detection Mechanism of Self-Assembling 19F NMR/MRI Nanoprobes toward Rational Design and Improved Sensitivity. J. Am. Chem. Soc. 2011, 133 (30), 11725–11731. [PubMed: 21699190]

(36). Wang H; Raghupathi KR; Zhuang J; Thayumanavan S Activatable Dendritic ^{19}F Probes for Enzyme Detection. ACS Macro Lett. 2015, 4 (4), 422–425. [PubMed: 25949857]

(37). Zheng M; Wang Y; Shi H; Hu Y; Feng L; Luo Z; Zhou M; He J; Zhou Z; Zhang Y; et al. Redox-Mediated Disassembly to Build Activatable Trimodal Probe for Molecular Imaging of Biothiols. ACS Nano 2016, 10 (11), 10075–10085. [PubMed: 27934082]

(38). Wang K; Peng H; Thurecht KJ; Puttick S; Whittaker AK Segmented Highly Branched Copolymers: Rationally Designed Macromolecules for Improved and Tunable 19F MRI. Biomacromolecules 2015, 16, 2827–2839. [PubMed: 26218187]

(39). Knight JC; Edwards PG; Paisey SJ Fluorinated Contrast Agents for Magnetic Resonance Imaging; a Review of Recent Developments. RSC Adv. 1, 1415–1425.

(40). Ryu JH; Jiwpanich S; Chacko R; Bickerton S; Thayumanavan S Surface-Functionalizable Polymer Nanogels with Facile Hydrophobic Guest Encapsulation Capabilities. J. Am. Chem. Soc. 2010, 132 (24), 8246–8247. [PubMed: 20504022]

(41). Ryu JH; Bickerton S; Zhuang J; Thayumanavan S Ligand-Decorated Nanogels: Fast One-Pot Synthesis and Cellular Targeting. Biomacromolecules 2012, 13 (5), 1515–1522. [PubMed: 22455467]

(42). Aktan B; Chambre L; Sanyal R; Sanyal A "Clickable" Nanogels via Thermally Driven Self-Assembly of Polymers: Facile Access to Targeted Imaging Platforms Using Thiol–Maleimide Conjugation. Biomacromolecules 2017, 18 (2), 490–497. [PubMed: 28052673]

(43). Munkhbat O; Garzoni M; Raghupathi KR; Pavan GM; Thayumanavan S Role of Aromatic Interactions in Temperature-Sensitive Amphiphilic Supramolecular Assemblies. Langmuir 2016, 32 (12), 2874–2881. [PubMed: 26938461]

(44). Ryu JH; Lee S; Son S; Kim SH; Leary JF; Choi K; Kwon IC Theranostic Nanoparticles for Future Personalized Medicine. J. Controlled Release 2014, 190, 477–484.

(45). Janib SM; Moses AS; Mackay JA Imaging and Drug Delivery Using Theranostic Nanoparticles. Adv. Drug Delivery Rev. 2010, 62 (11), 1052–1063.

(46). Xie J; Lee S; Chen X Nanoparticle-Based Theranostic Agents. Adv. Drug Delivery Rev. 2010, 62 (11), 1064–1079.

(47). Chen G; Qiu H; Prasad PN; Chen X Upconversion Nanoparticles: Design, Nanochemistry, and Applications in Theranostics. Chem. Rev. 2014, 114, 5161–5214. [PubMed: 24605868]

(48). Chambre L; Degirmenci A; Sanyal R; Sanyal A Multi-Functional Nanogels as Theranostic Platforms: Exploiting Reversible and Nonreversible Linkages for Targeting, Imaging, and Drug Delivery. Bioconjugate Chem. 2018, 29 (6), 1885–1896.

(49). Low PS; Henne WA; Doorneweerd DD Discovery and Development of Folic-Acid-Based Receptor Targeting for Imaging and Therapy of Cancer and Inflammatory Diseases. Acc. Chem. Res. 2008, 41 (1), 120–129. [PubMed: 17655275]

(50). Lu Y; Low PS Folate-Mediated Delivery of Macromolecular Anticancer Therapeutic Agents. Adv. Drug Delivery Rev. 2012, 64, 342–352.

(51). Hilgenbrink AR; Low PS Folate Receptor-Mediated Drug Targeting: From Therapeutics to Diagnostics. J. Pharm. Sci. 2005, 94 (10), 2135–2146. [PubMed: 16136558]
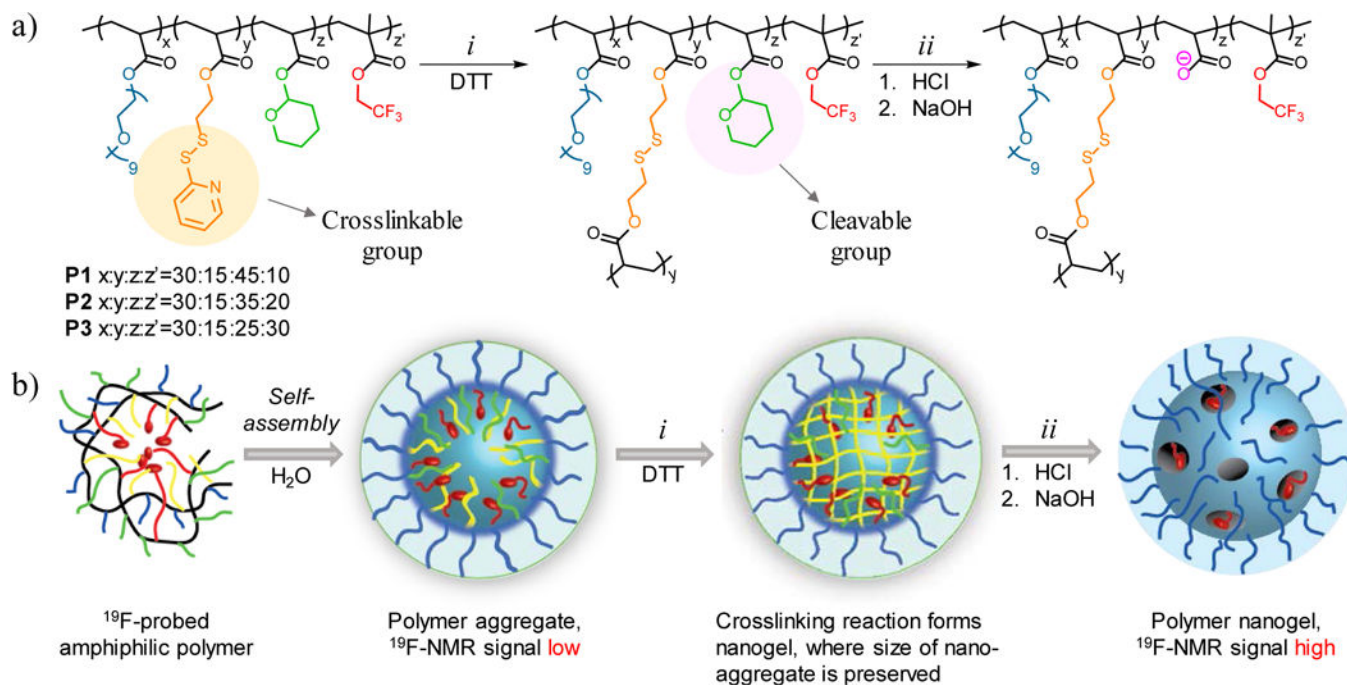
Figure 1.
Design and synthesis of fluorinated probe. (a) Structure of polymer and nanogel. (*i*) Nanogel formation via crosslinking of PDS groups with DTT (*ii*) Cleavage of THP group in the presence of HCl and formation of negatively charged moiety with NaOH addition. (b) Schematic representation of preparation of fluorinated nanogel with decreased interior density.
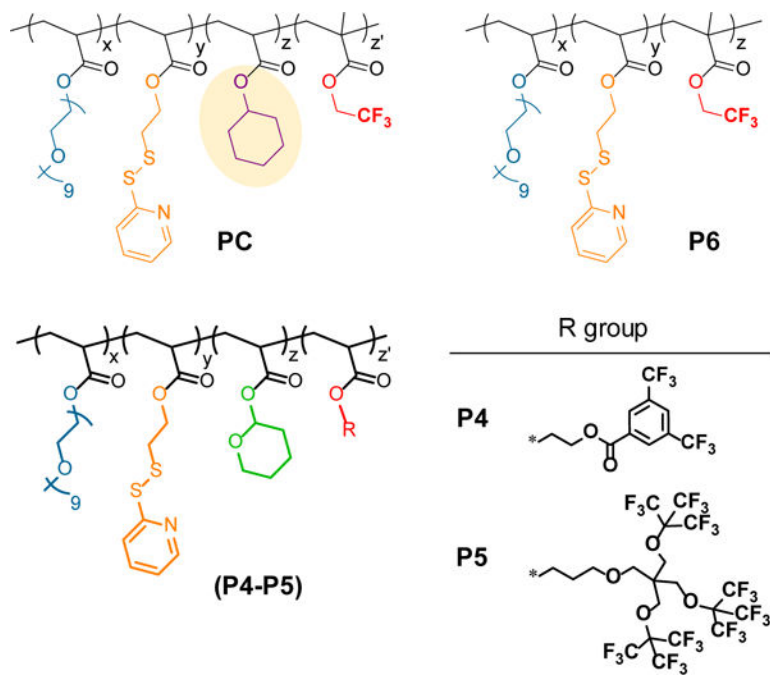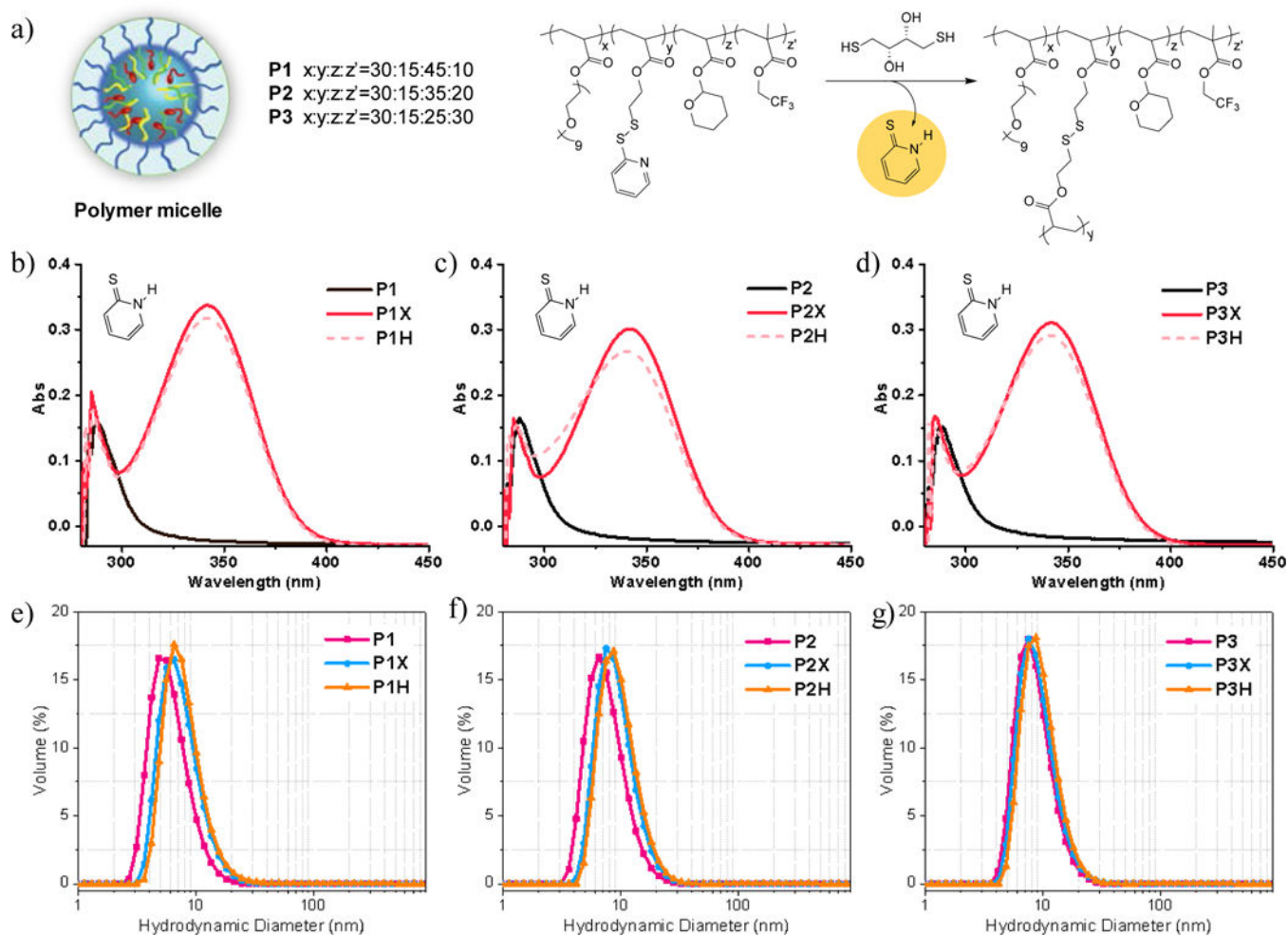
Figure 2.
Structure of control polymers tested in this study

Figure 3.
(a) DTT crosslinking reaction of polymer assembly. (b) Absorption spectra of pyridothione at 342 nm, confirming the formation of polymer nanogel. (e) Size distribution of polymer assembly, polymer nanogel and acid degraded polymer nanogel of **P1**-**P3**.
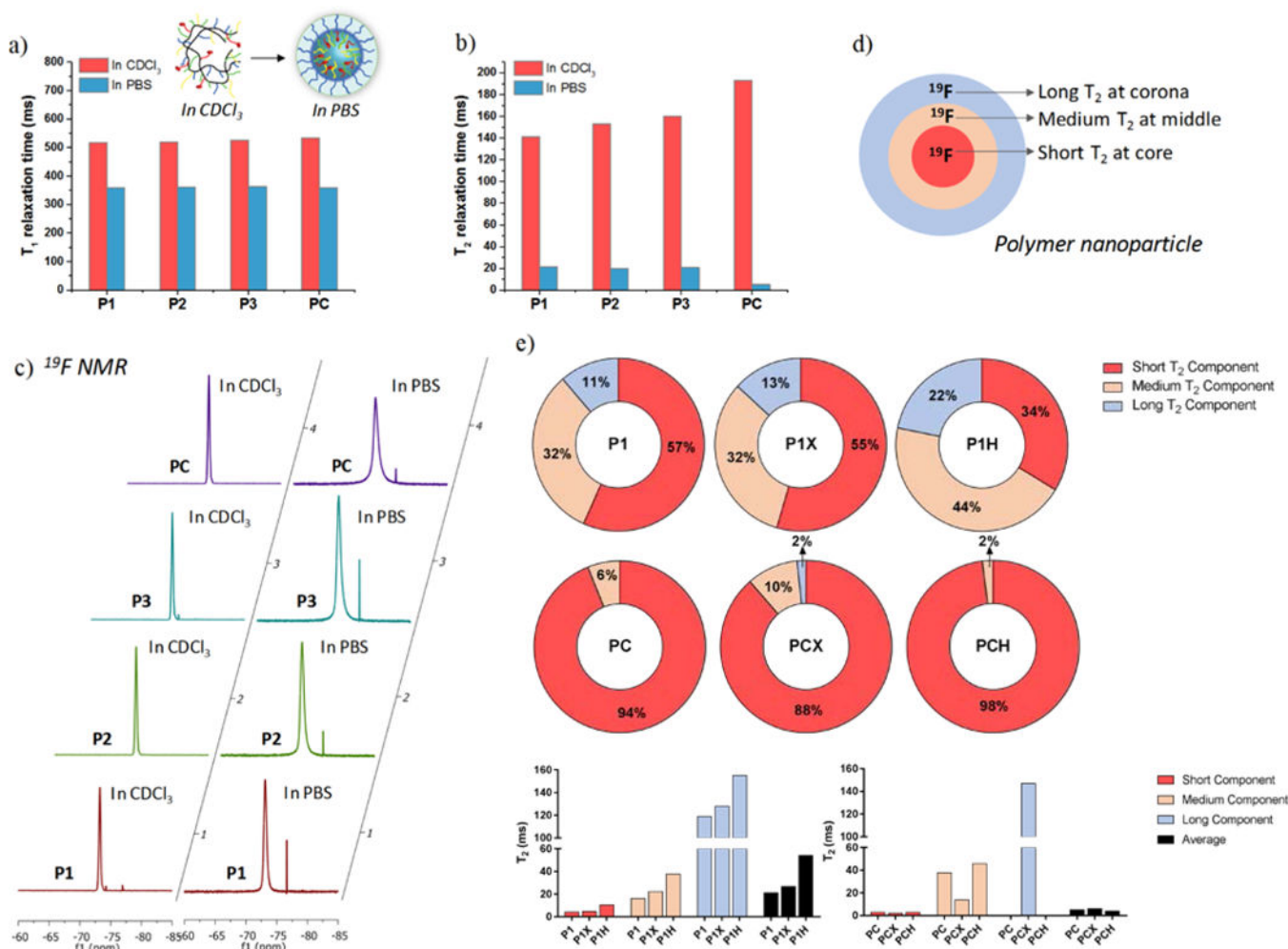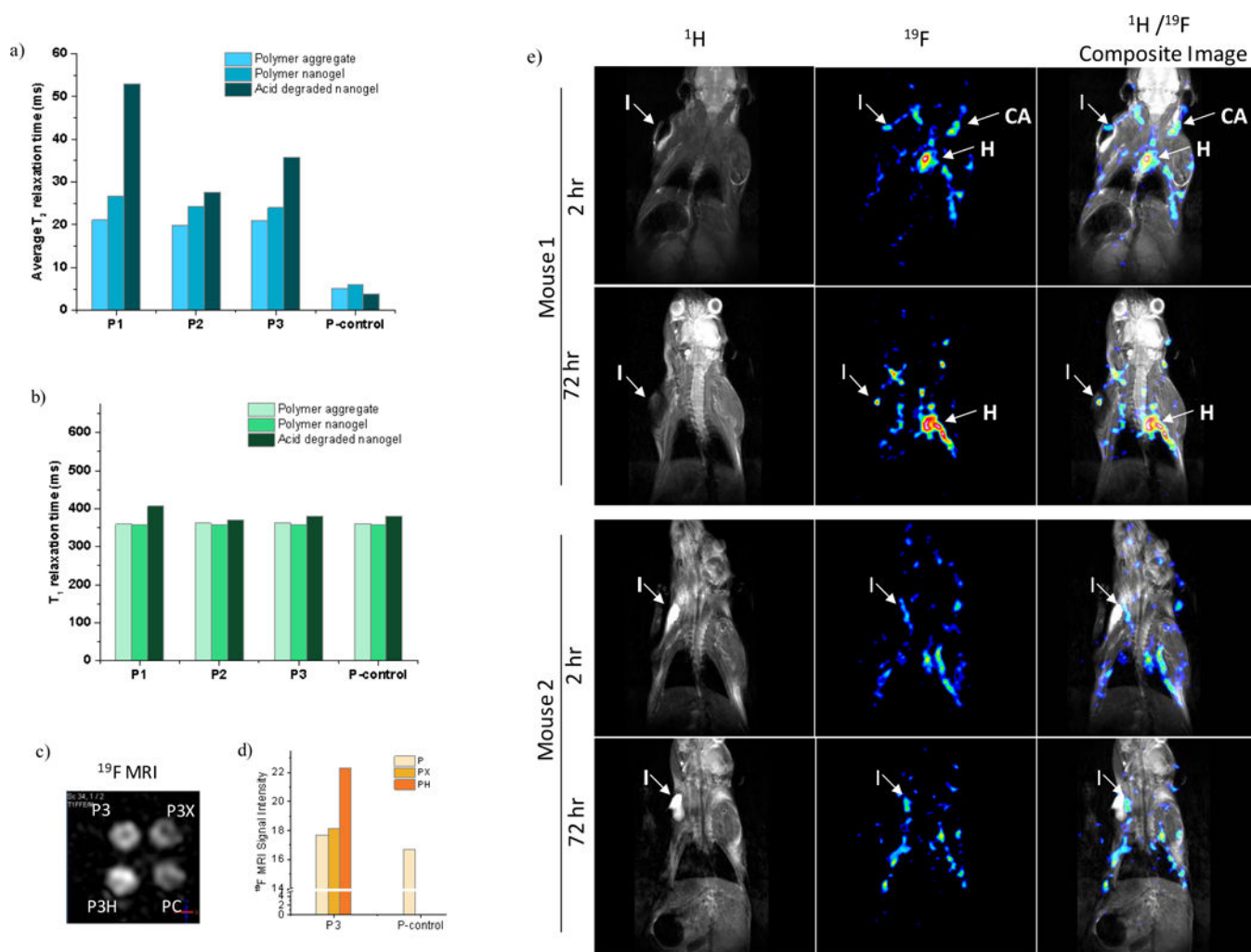
Figure 4.
Change of ^{19}F NMR relaxation times in polymers upon aggregation: (a) Decrease of T_1 in PBS buffer. (b) Decrease of average T_2 in PBS buffer. (c) ^{19}F NMR peak broadening in aqueous solution versus organic solvent. (d) Variation of T_2 depending on the fluorine microenvironment. (e) Evolution of T_2 in **P1** and **PC** upon DTT crosslinking and acid degradation. Graph is designed to represent the increase of T_2 value for all component, increase of relative intensity for the longer T_2 component and the decrease of relative intensity for the shorter T_2 component resulting in increased overall T_2 value. Similar trend is observed for both **P2** and **P3** upon acid treatment.

Figure 5.
(a) Evolution of average T_2 for all polymers. (b) Evolution of T_1 for all polymers. (c,d) ^{19}F phantom MRI image of **P3** series. (e) *in vivo* MRI showing the accumulation of P3H at the site of inflammation over 72 hours. The ^1H coronal images are represented in grayscale, the ^{19}F is in 16 color intensity scale. (I: inflammation, CA: carotid arteries, H: heart).
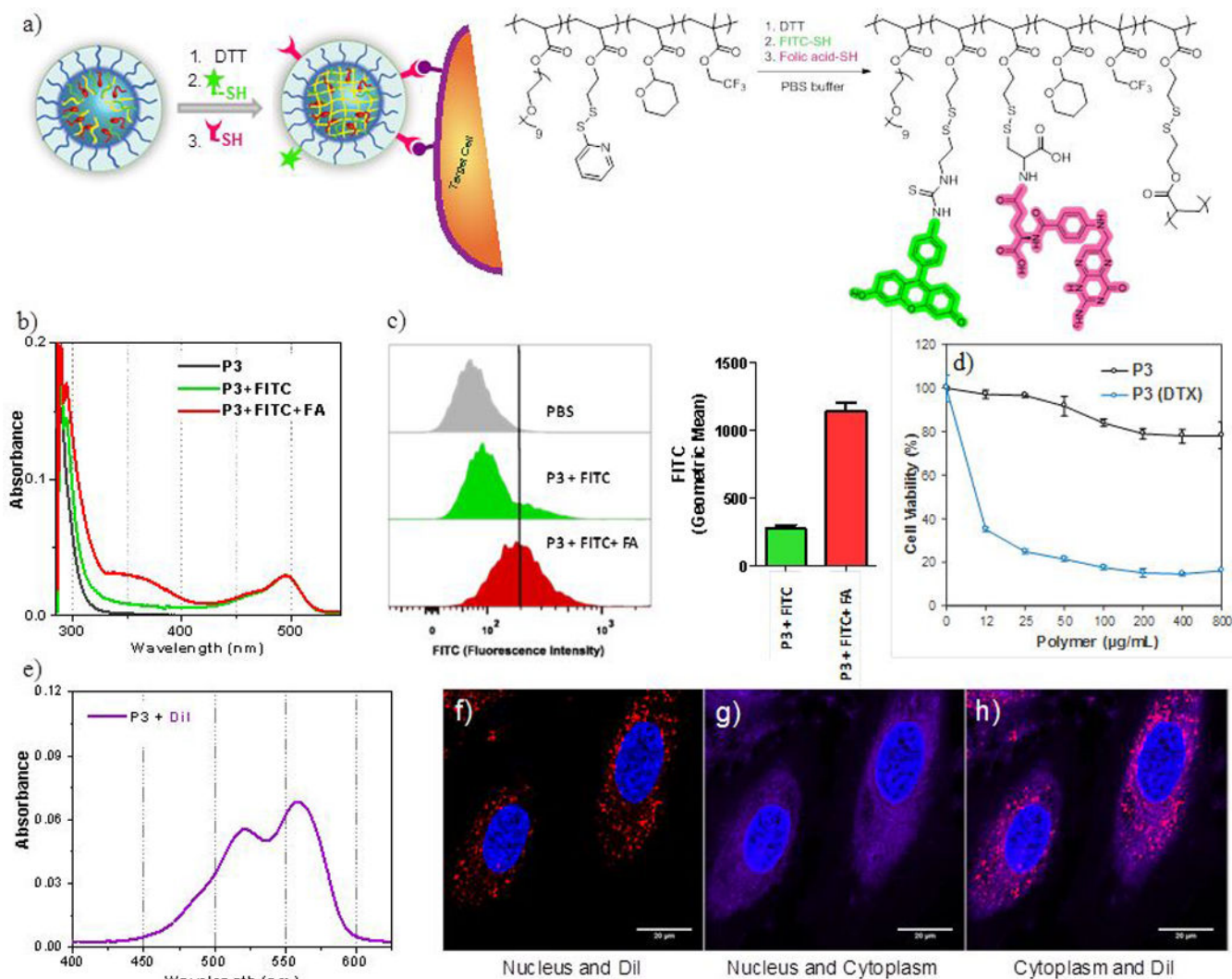
Figure 6.

Post-modification of nanogel. (a) Surface functionalization of nanogel with FITC and FA through disulfide exchange reaction. (b) UV absorption spectrum of **P3** before and after surface modification. (c) Flow cytometry analysis of HeLa cells after the incubation with **P3** with and without FA-conjugation. (d) MTT cell viability assay using HeLa cells incubated with empty and docetaxel encapsulated **P3**. (e) UV absorption spectrum of DiI encapsulation to **P3**. (f-h) Confocal microscopy imaging of HeLa cells incubated with DiI encapsulated in **P3** nanogels. DiI is shown in red, nucleus in blue, and cytoplasm in magenta.

Table 1.

Evolution of T_2 relaxation time with the respect to crosslinking and the acid degradation in **P1, P2, P3** and **PC**.

	Component 1		Component 2		Component 3		Avg. T_2(ms)
	T_2(ms)	Int. %	T_2(ms)	Int. %	T_2(ms)	Int. %	
P1	4.3	56.7	16.2	32.0	119	11.3	21.1
P1X	4.8	54.5	22.1	32.3	128	13.2	26.7
P1H	10.4	33.7	37.8	44.5	155	21.8	54.1
P2	3.8	62.3%	16.8	27.9%	130	9.8%	19.8
P2X	4.2	60.3%	22.0	28.1%	134	11.6%	24.3
P2H	4.3	54.3%	22.1	32.4%	137	13.3%	27.7
P3	3.8	65.5%	18.5	25.0%	146	9.5%	21.0
P3X	3.7	61.5%	20.6	26.7%	138	11.8%	24.1
P3H	5.7	47.5%	27.5	36.5%	144	16.0%	35.8
PC	3.0	93.9%	37.7	6.1%	-	-	5.1
PCX	2.5	88.6%	14.0	9.7%	147	1.7%	6.1
PCH	3.0	98.0%	46.0	2.0%	-	-	3.9